

# Mid-Infrared Quartz-Enhanced Photoacoustic Sensor for ppb-Level CO Detection in a SF<sub>6</sub> Gas Matrix Exploiting a T-Grooved Quartz Tuning Fork

Bo Sun, Andrea Zifarelli, Hongpeng Wu,\* Stefano Dello Russo, Shangzhi Li, Pietro Patimisco, Lei Dong,\* and Vincenzo Spagnolo\*



Cite This: *Anal. Chem.* 2020, 92, 13922–13929



Read Online

ACCESS |



Metrics & More

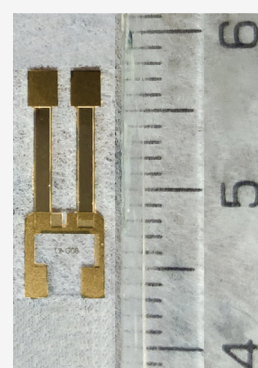


Article Recommendations



Supporting Information

**ABSTRACT:** An optical sensor for highly sensitive detection of carbon monoxide (CO) in sulfur hexafluoride (SF<sub>6</sub>) was demonstrated by using the quartz-enhanced photoacoustic spectroscopy technique. A spectrophone composed of a custom 8 kHz T-shaped quartz tuning fork with grooved prongs and a pair of resonator tubes, to amplify the laser-induced acoustic waves, was designed aiming to maximize the CO photoacoustic response in SF<sub>6</sub>. A theoretical analysis and an experimental investigation of the influence of SF<sub>6</sub> gas matrix on spectrophone resonance properties for CO detection have been provided, and the performances were compared with the standard air matrix. A mid-infrared quantum cascade laser with a central wavelength at 4.61 μm, resonant with the fundamental band of CO, and an optical power of 20 mW was employed as the light excitation source. A minimum detection limit of 10 ppb at 10 s of integration time was achieved, and a sensor response time of ~3 min was measured.



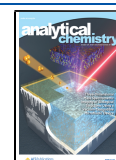
Sulfur hexafluoride (SF<sub>6</sub>) is a nontoxic, nonflammable, and thermally stable gas with excellent heat transfer and arc-quenching capability.<sup>1</sup> The latter comes from the ability of SF<sub>6</sub> molecules to rapidly recombine after dissociation during an electrical discharge, providing a strong dielectric recovery strength. Therefore, SF<sub>6</sub> is widely used as a gas-insulating medium in several high-voltage apparatuses, including gas-insulated switchgears (GISs), gas circuit breakers, and gas-insulated transformers. These devices have become the main equipment of electrical power stations because of their high insulation reliability, low failure rate, and small footprint.<sup>2</sup> However, because of the aging, internal diagnosis and rapid maintenance are essential to improve the reliability of its power supply, especially for large-scale GIS equipment.<sup>3</sup> Several kinds of local insulation defects existing in GISs, such as spark and arc discharges, can cause decomposition reactions of SF<sub>6</sub>.<sup>4,5</sup> Although its decomposition temperature is 500 °C, when SF<sub>6</sub> coexists with metals, different decompositions may occur also at 200 °C to generate a variety of low-fluorine sulfides such as SF<sub>4</sub>, SF<sub>2</sub>, and S<sub>2</sub>F<sub>10</sub>.<sup>6</sup> These low-fluorine sulfides react with moisture and oxygen and generate chemically active by-products such as CO, SO<sub>2</sub>, H<sub>2</sub>S, CF<sub>4</sub>, and so forth,<sup>7,8</sup> with different contents and ratios. Thus, the detection of SF<sub>6</sub> gas decomposition products can be an efficient method for equipment failure detection, especially if the detection technique is not affected by electromagnetic noise and mechanical vibrations, making it suitable for *in situ* detection. The early detection of partial discharges could allow predicting overheating faults, as well as to check whether the internal

insulation materials in electrical equipment are qualified.<sup>9</sup> Among these decomposition products, carbon monoxide (CO) is a trace characteristic component that can be used as an indicator gas to identify low-temperature overheating insulation defects in GIS equipment. Excessive CO generated inside the equipment also poses a threat to personnel safety issues. When the CO concentration is within 20 parts-per-million (ppm), it means that the GIS is working in a safe state.<sup>10</sup> When it exceeds this range, the equipment should be maintained in time. Therefore, it is crucial to develop and design a compact, highly stable, and sensitive CO gas sensor for GISs that can detect the CO concentration in the SF<sub>6</sub> matrix with a detection limit below 1 ppm in real time. Some methods for measuring the content of decomposition products of SF<sub>6</sub>, such as gas chromatography,<sup>11</sup> electrochemical method,<sup>12</sup> metal-oxide semiconductor sensors,<sup>13</sup> and tube detection method<sup>14</sup> have been reported. However, these methods suffer from poor stability, long stabilization time, large background noise, and material consumption. Recently, optical methods have been used for the detection of decomposition products of SF<sub>6</sub>, and several CO optical sensors

Received: June 29, 2020

Accepted: September 23, 2020

Published: September 23, 2020



in SF<sub>6</sub> have been reported. In 2018, a tunable diode laser absorption spectroscopy sensor employing a diode laser emitting at 2.33  $\mu\text{m}$  and a 14.5 m multipass gas cell allowed CO detection at ppm level.<sup>9</sup> In 2019, a photoacoustic spectroscopy (PAS) sensor was developed to detect the CO content in SF<sub>6</sub> in real time. Employing a DFB laser emitting at 1.56  $\mu\text{m}$  together with a 10 W fiber amplifier, a minimum CO detection limit of  $\sim 120$  ppb was achieved.<sup>15</sup>

Quartz-enhanced PAS (QEPAS) has established itself as an enhanced version of traditional PAS,<sup>16</sup> with further advantages of low-cost, high immunity to external noise, and small compact volumes,<sup>17–19</sup> in which the wideband microphone of traditional PAS is replaced with an ultra-narrowband quartz tuning fork (QTF) to detect sound waves generated when the gas absorbs modulated light. The QTF is acoustically coupled with a pair of millimeter-size resonator tubes, aligned on both sides of the QTF in a way that the laser beam can be focused between QTF prongs while passing through both tubes, without touching them.<sup>20–22</sup> When the laser beam is modulated at the resonance frequency of one in-plane flexural mode of the QTF, a standing wave vibrational pattern is created within the resonator tubes, which deflects the two prongs in opposite directions, exciting QTF piezoelectrically active, antisymmetrical flexural mode. Thus, an electrical signal proportional to the absorbing analyte concentration is generated. From 2002, several QEPAS sensors have been realized and more than 30 different analytes have been detected by using various wavelength laser sources, spanning from UV–visible to terahertz range, in most cases with ultimate detection limits in parts-per-billion range.<sup>20</sup> The QTF resonance frequency rules the modulation of the absorbed light, which in turn determines the efficiency of the energy relaxation, that is, the efficiency of sound generation.<sup>23</sup> With a commercial QTF having a frequency as high as 32.7 kHz, the energy relaxation occurring in the absorbing gas cannot be fast enough to follow the intensity light modulation, resulting in low radiation-to-sound conversion efficiency. In fact, CO has a relatively slow vibration-to-translational (V–T) energy-transfer rate, which leads to a weak QEPAS signal output when a 32.7 kHz QTF is employed. These issues promote the research of the QTF with lower resonance frequencies.<sup>24,25</sup> In all sensors reported in the literature, trace analyte was detected in N<sub>2</sub> or air matrix. A CO QEPAS sensor in the air matrix was demonstrated by exploiting a custom-made 15.2 kHz-QTF with grooves carved on both prongs' surfaces. With water vapor as the catalyst for vibrational energy transfer, the QEPAS sensor reached a minimum detection limit of 7 ppb for a 1 s averaging time.<sup>26</sup> When the gas matrix changes, two considerations should be taken into account. First, the main energy dissipation mechanism occurring in a vibrating prong is the damping by the surrounding fluid.<sup>27</sup> Thus, the matrix composition and its thermodynamic parameters affect the QTF quality factor. Because the QEPAS signal is proportional to the QTF quality factor, the ultimate sensor sensitivity will be dependent on the matrix composition. For gas matrices composed by molecules with heavy molecular weight, such as the SF<sub>6</sub> matrix, the drop of the QTFs' quality factor due to damping effects may strongly affect the sensor performances. The second consideration regards the geometrical parameters of resonator tubes, in particular, the internal diameter and the length of the two tubes  $l$ , that influence the sensor performance.<sup>21,22</sup> The length of the two tubes is correlated with the sound wavelength  $\lambda = \nu_s/f_0$ , where  $\nu_s$  is the sound

speed in the matrix and  $f_0$  is the QTF resonance frequency. Because  $\nu_s$  depends on matrix temperature and composition, the tube length must be optimized for the SF<sub>6</sub> matrix to match the acoustic field inside the tubes. All these considerations suggest that the QEPAS spectrophone composed by the QTF and resonator tubes must be properly designed and optimized for an efficient CO detection in the SF<sub>6</sub> matrix.

In this paper, a custom T-shape QTF with grooves carved on the prong surface was designed with a resonance frequency of 8 kHz, 4 times lower than the standard QTF, and a quality factor of  $\sim 11,000$  in air, at atmospheric pressure. By means of this QTF, the QEPAS technique was applied to the measurement of CO in the SF<sub>6</sub> environment. The geometric parameters of tubes were studied to ensure high sound amplification in the SF<sub>6</sub> matrix. The QEPAS spectrophone performance was analyzed both in standard air and in the SF<sub>6</sub> matrix. A mid-infrared distributed-feedback (DFB) quantum cascade laser (QCL) with a center wavelength of 4.61  $\mu\text{m}$  was chosen as the light source to photoacoustically excite the CO molecules.

## ■ EXPERIMENTAL SECTION

**CO Relaxation Dynamics in the SF<sub>6</sub> Matrix.** CO is a heavy diatomic molecule with a low density of vibrational energy levels. Therefore, the CO molecule is characterized by a slow V–T energy transfer rate in the collisional de-excitation process with another CO molecule as well as in the collision with a N<sub>2</sub> molecule. Indeed, the QEPAS sensor based on commercial 32.7 kHz-QTF allowed the ultimate detection limit of CO at parts-per-billion concentration level but with a watt-level excitation source.<sup>28</sup> Furthermore, SF<sub>6</sub> has a high density of vibrational levels available for multichannel resonant energy transfers *via* consecutive multistep relaxation processes. For this reason, SF<sub>6</sub> has been widely used as a promoter for slow-relaxing gases, such as N<sub>2</sub>O and CO<sub>2</sub>, in order to speed up the relaxation processes and increase the QEPAS sensor response. Although it is efficient in case of N<sub>2</sub>O and CO<sub>2</sub>, SF<sub>6</sub> does not significantly promote vibrational de-excitation of CO.<sup>29</sup> Thus, SF<sub>6</sub> does not act as a relaxation promoter for CO. The CO QEPAS signal can be expressed as

$$S = \frac{S_0}{\sqrt{1 + \left(\frac{2\pi f\tau}{P}\right)^2}} \quad (1)$$

where  $f$  is the QTF resonance frequency,  $\tau$  is the gas sample effective relaxation time,  $P$  is the operating pressure, and  $S_0$  is the photoacoustic signal for instantaneous V–T transfer, that is, where  $f\tau/P \ll 1$ . The CO relaxation time  $\tau$  in a SF<sub>6</sub> matrix depends on the different collision channels with the different types of molecules in the mixture.

The excited CO molecules can relax in a nonradiative way by V–T collisions with another CO molecule (identified by a characteristic relaxation time  $\tau_{V-T}$ ) or, alternatively, by V–V (vibrational to vibrational) interaction with an SF<sub>6</sub> molecule ( $\tau_{V-V}$ ), which will be in turn excited. This excited SF<sub>6</sub> molecule will consequently de-energize by V–T collisions with other SF<sub>6</sub> molecules ( $\tau_{V-T, \text{SF}_6}$ ). The potential relaxation pathways of the laser-excited CO energy level are shown in Figure 1.

The relaxation time values reported in the literature are  $\tau_{V-T, \text{SF}_6} = 42 \mu\text{s Torr}$ ,<sup>30</sup>  $\tau_{V-V} = 33 \text{ ms Torr}$ ,<sup>31</sup> and  $\tau_{V-T} = 1.52 \text{ ms Torr}$ .<sup>32</sup>  $\tau_{V-T, \text{SF}_6}$  is 3 orders of magnitude smaller than  $\tau_{V-V}$ ,

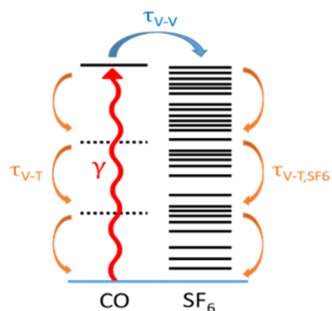


**Figure 1.** Relaxation pathways following optical excitation (represented by the red wavy arrow) of the excited level of CO molecules.

and therefore, V–T collisions between SF<sub>6</sub> molecules can be considered as instantaneous. The relaxation rate  $1/\tau$  is then given by the sum of the relaxation rates of every possible energy-transfer pathway, weighted by the concentrations of CO and SF<sub>6</sub> molecules,  $C_{\text{CO}}$ , and  $C_{\text{SF}_6}$ , respectively, in the mixture by<sup>33</sup>

$$\frac{1}{\tau} = \frac{C_{\text{CO}}}{\tau_{\text{V-T}}} + \frac{C_{\text{SF}_6}}{\tau_{\text{V-T}}} \quad (2)$$

The effective relaxation time of CO in the SF<sub>6</sub> matrix is  $\tau = 33$  ms Torr. With such a high value, the ratio  $S/S_0$  is  $\sim 0.11$  when a standard 32 kHz QTF is employed at atmospheric pressure but can increase up to  $\sim 0.42$  if the QTF resonance frequency is reduced to 8 kHz.

**Design and Test of the QEPAS Spectrophone.** In ref 26, a custom 15.2 kHz-QTF with rectangular grooves was used for the spectrophone of QEPAS sensor for CO detection in air. The prong length  $l$ , width  $w$ , thickness  $t$ , and prong spacing  $g$  of the 15.2 kHz-QTF are 9.4, 2, 0.25, and 0.8 mm, respectively. In addition, four 50  $\mu\text{m}$  deep rectangular grooves were carved on both surfaces of the two QTF prongs in order to decrease the QTF electrical resistance.<sup>34</sup> The fundamental mode at 15,243 Hz reaches a quality factor of 15,020 at atmospheric pressure, in air. Moving to low resonance frequencies by varying the ratio  $t/l$  following Euler–Bernoulli equation for rectangular prongs, the  $Q$ -factor decreases. In particular, QTFs with a resonance frequency lower than 10 kHz cannot ensure  $Q > 10,000$ , at atmospheric pressure. A further reduction of resonance frequency with slight modifications of the overall quality factor requires a change of prong geometry. T-shaped prongs have been proposed to accomplish both requirements,

with a further increase of stress field distribution along the vibrating prongs with respect to the rectangular prongs, beneficial for piezoelectric charge generation when the prongs are deflected.

To investigate the resonance properties of a T-shaped grooved QTF, a finite-element-analysis (FEA) using COMSOL Multiphysics was performed.  $T_1$  represents the width of the T-shaped prong head and  $T_2$  represents the width of the T-shaped prong body (see Figure 2a). The influence of the ratio  $T_2/T_1$  on the resonance frequency was investigated.  $T_1$ ,  $L_1$ , and  $L_2$  were kept constant to 2.0, 2.4, and 7.0 mm, respectively, as for 15.2 kHz-QTF in ref 26, while  $T_2$  was reduced. Fifty micrometer deep grooves were carved on both sides of each prong, as sketched in Figure 2a. The simulation was performed in a vacuum environment to avoid the influence of the surrounding medium, and the results are shown in Figure 2b.  $T_2/T_1 = 0.5$  was set as the lower limit for the simulation.

The simulation results clearly indicate a linear trend of the fundamental resonance frequencies with respect to the  $T_2/T_1$  ratio, with an  $R^2$  value of 0.9998. Ratios lower than 0.7, that is,  $T_2$  smaller than 1.4 mm, lead to resonance frequencies lower than 10 kHz. However, the lowering of the resonance frequency through the reduction of  $T_2/T_1$  ratio is in competition with the mechanical stability of the QTF. Low  $T_2/T_1$  ratio would not guarantee a stable oscillation of the QTF prong because of the low moment of inertia. Moreover, prong oscillations would be highly influenced by the surrounding medium damping, leading to high viscous losses that in turn negatively affect the quality factor.<sup>27</sup> For these reasons, the ratio  $T_2/T_1 = 0.6$  was chosen, corresponding to  $T_1 = 2.0$  mm and  $T_2 = 1.2$  mm. The predicted fundamental resonance frequency in vacuum is equal to 7903 Hz.

Based on this simulation, we realized a QTF as reported in ref 23. The resonance properties of the QTF fundamental mode were measured by using the electric excitation experimental setup (Figure S1 of the Supporting Information). The QTF is mounted in an airtight chamber, connected with a gas line that included a pressure controller, a valve system, and an oil-free pump. In this way, it is possible to select and fix the gas pressure in the chamber in the range between 50 and 700 Torr. For each pressure, resonance curves were acquired by varying step-by-step the frequency of the function generator. Each resonance curve was fitted by a Lorentzian function to determine the resonance frequency, that is, the peak value of the Lorentzian fit function and the full-width-half-maximum (fwhm). The ratio between the resonance frequency and the

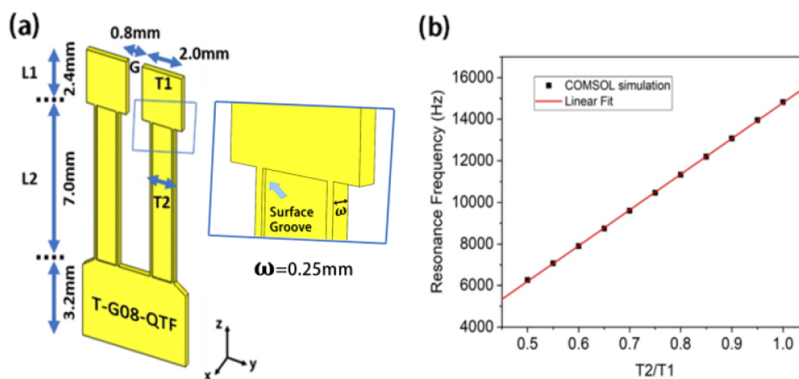


**Figure 2.** (a) Schematic diagram of the T-shaped grooved QTF, with geometrical parameters. (b) COMSOL Multiphysics simulation of the fundamental resonance frequency of T-shaped grooved QTF as a function of the  $T_2/T_1$  ratio.



fwhm value gives the QTF quality factor. The resonance curves at different pressures were acquired with two different gases flowing in the chamber, standard air and pure SF<sub>6</sub>. The resonance frequencies  $f_0$  are plotted as a function of the pressure in Figure 3, when standard air (red circles) or pure SF<sub>6</sub> (blue squares) flows in the chamber.

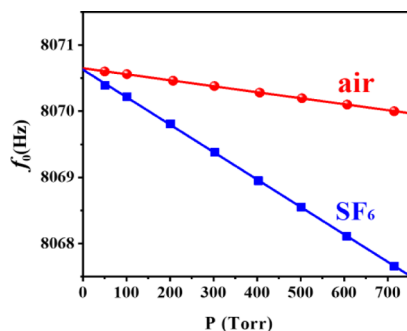


**Figure 3.** Measured fundamental resonance frequency for QTF in ambient air (red circles) and in pure SF<sub>6</sub> (blue squares) as a function of the QTF operating pressure.

For both gases, the QTF resonance frequency linearly decreases as the pressure increases. The dependence of the resonance frequency on the surrounding gas pressure can be determined by the assumption that the gas effect on prong vibrations damping increases the inertia of the prong. Thus, the Euler–Bernoulli equation describing the motion of a vibrating prong requires an additional term corresponding to the reactive part, which attributes additional inertia to the vibrating prong<sup>23,35</sup>

$$EI \frac{\partial^4 y(z, t)}{\partial z^4} + (\rho A + u) \frac{\partial^2 y(z, t)}{\partial t^2} = 0 \quad (3)$$

where  $E$  is the quartz Young modulus,  $I$  is the moment of inertia of the prong,  $A$  is the cross-sectional area of the prong,  $u$  is the added mass,  $\rho$  is the quartz density,  $t$  is the time, and  $y(z)$  is the prong displacement function. eq 3 can be solved by imposing clamped-free boundary conditions (i.e., one prong end is free to oscillate while the other end is clamped to the quartz base) and eigen frequencies  $f$  can be estimated as<sup>35</sup>

$$f = f_0 \left( 1 - \frac{1}{2} \frac{u}{\rho A} \right) \quad (4)$$

where  $f_0$  is the resonance frequency in vacuum, that is, the first eigen frequency (referred to the fundamental flexural mode) of eq 3 when  $u = 0$ . The exact derivation of the added mass  $u$  is a complicated problem even for simple prong structures. In ref 36, the added mass per unit length of a thin beam of width  $w$  has been found to be proportional to gas density  $\rho_0$ . By using the ideal gas law, the gas density can be expressed by

$$\rho_0 = \frac{MP}{RT} \quad (5)$$

where  $M$  is the molar mass,  $P$  is the gas pressure (in Torr unit),  $R = 62.3637 \text{ m}^3 \text{ Torr/kmol}$  is the gas constant, and  $T$  is the prong temperature (in K). Thus, the frequency shift of the QTF resonance frequency because of a pressure change depends on the molar mass of the gas mixture, if the temperature is fixed. Following these considerations, the data points of Figure 3 have been fitted by a linear function, resulting in  $f = 8070.65 - k_{\text{air}} \cdot P$  and  $f = 8070.63 - k_{\text{SF}_6} \cdot P$  when the gas matrix is air or pure SF<sub>6</sub>, respectively, with  $k_{\text{air}} = 9.05 \times 10^{-4} \text{ Hz/Torr}$  and  $k_{\text{SF}_6} = 4.15 \times 10^{-3} \text{ Hz/Torr}$ . The intercept values are almost identical and represent the resonance frequency in vacuum, namely,  $f_0$  in eq 4, while different slope values have been recorded. The discrepancy between the measured  $f_0$  ( $\sim 8070.6 \text{ Hz}$ ) and the related FEA prediction (7903 Hz) can be ascribed to small deviations in geometry between the modeled and the real QTF and to additional weight because of the electrode gold layers, as well as to dependence of the elasticity modulus of quartz on the crystallographic axis orientation. The molar mass of SF<sub>6</sub>,  $M_{\text{SF}_6}$ , is 146.06 g/mol and that of the air,  $M_{\text{air}}$ , is 28.96 g/mol. According to eqs 4 and 5, the ratio  $k_{\text{SF}_6}/k_{\text{air}} = 4.6$  is comparable with  $M_{\text{SF}_6}/M_{\text{air}} = 5.0$ , demonstrating that the QTF frequency shift as a function of the pressure are mainly dominated by the mass of the surrounding gas, which is a bulk property.

The Q-factor of a resonance mode is a measure of the energy loss of prongs while it is vibrating.<sup>27,37</sup> It has been demonstrated that the QTF mainly loses energy via the interaction with the surrounding viscous medium. The air damping mechanism can be modeled by using an analytical expression derived by Hosaka *et al.*<sup>38</sup> leading to a formulation of the Q-factor contribution related to gas damping

$$Q_{\text{gas}} \approx \frac{4\rho T_2 w^2 f}{3\mu w + \frac{3}{4} w^2 \sqrt{4\pi\rho_0 \mu f}} \quad (6)$$

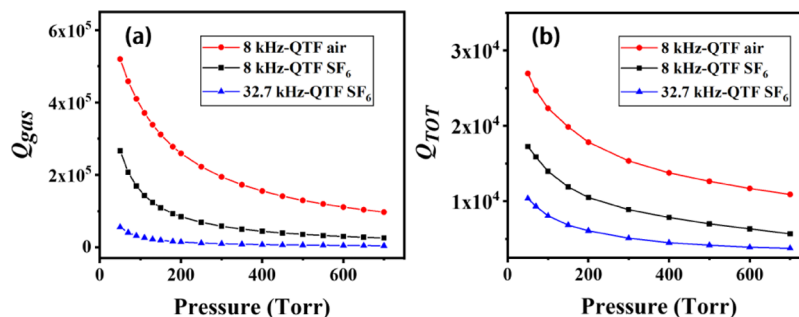


**Figure 4.** (a) Simulation of fluid damping-related Q-factor ( $Q_{\text{gas}}$ ) as a function of operating pressure for standard QTF in SF<sub>6</sub> (blue triangles) and for the custom T-shaped QTF employed in this work for both SF<sub>6</sub> (black squares) and air (red dots). (b) Measured total Q-factor ( $Q_{\text{TOT}}$ ) as a function of operating pressure for standard QTF in SF<sub>6</sub> (blue triangles) and for the custom T-shaped QTF employed in this work for both SF<sub>6</sub> (black squares) and air (red dots).

where  $\mu$  is the gas viscosity. By combining eqs 3 and 4 and using experimental resonance frequency values reported in Figure 3,  $Q_{\text{gas}}$  has been plotted as a function of the gas pressure both for air ( $\mu = 1.81 \times 10^{-5}$  kg/m s) and  $\text{SF}_6$  ( $\mu = 1.4 \times 10^{-5}$  kg/m s) in Figure 4a. The same trend has been also simulated for standard 32.7 kHz in  $\text{SF}_6$  ( $T_2 = 300$   $\mu\text{m}$ ,  $w = 350$   $\mu\text{m}$  and assuming a pressure-independent resonance frequency of 32.78 kHz). In Figure 4b, the measured quality factors are reported for the custom 8 kHz-QTF, in air and  $\text{SF}_6$ , and for standard 32.7 kHz-QTF.

The dependence of the measured  $Q$ -factors on gas pressure follows the trend of  $Q_{\text{gas}}$ , confirming that the dominant loss mechanism is gas damping, both for air and  $\text{SF}_6$ . Because of the heavy molecular weight of  $\text{SF}_6$ , for 8 kHz-QTF vibrating in  $\text{SF}_6$ , the quality factor is reduced in the overall pressure range with respect to the QTF immersed in air, while maintaining the same trend. When a standard 32.7 kHz-QTF is employed in  $\text{SF}_6$ , the quality factor values are well below the 8 kHz-QTF trend: in particular, at 500 Torr the quality factor is below 5000, not an optimal condition for a QTF to be used in a QEPAS sensor.

The QTF is not used as a standalone in a QEPAS sensor, but it is acoustically coupled with a pair of millimeter-size resonator tubes, typically located on both sides of the QTF (Figure S2). Resonator tubes act as an acoustic resonator:<sup>21,22</sup> the standing wave vibrational pattern within the tubes enhances the intensity of the acoustic field between the QTF prongs up to 60 times.<sup>34</sup> The QTF coupled with a pair of resonator tubes constitutes the QEPAS spectrophone and represents the core of any QEPAS detection module.

When acoustically coupled with a QTF, the internal diameter (ID) of tubes and their length influence the enhancement of the sound wave between QTF prongs. The optimal tube diameter can be estimated by considering the theoretical model proposed in ref 22, in which the acoustic coupling between two tubes is expressed in terms of the amount of the acoustic field transferred from one tube to the other one. As a result, the optimal tube radius strongly depends on the sound wavelength  $\lambda_s$  and prong spacing  $g$ . With an 8 kHz-QTF ( $\lambda_s = v_s/f_0 = 16.7$  mm, where the speed of sound in the  $\text{SF}_6$  gas is  $v_s = 136$  m/s and  $g = 800$   $\mu\text{m}$ ), the theoretical model predicts an optimal ID = 1.0 mm. The optimal tube length can be estimated by considering the open-end correction, which assumes that the antinode of a standing sound wave in an open-ended resonator is located outside the tube end because of an impedance mismatch between the acoustic field inside the resonator and outside. The optimal tube length  $l$  depends on the tube ID and the sound wavelength by the following relation<sup>39</sup>

$$l = \frac{v_s}{2f_0} - \frac{8\text{ID}}{3\pi} \quad (7)$$

For ID = 1.0 mm, the optimal theoretical length is 7.5 mm. These latter parameters will be used to assemble a dual-tube QEPAS spectrophone with the 8 kHz-QTF optimized to detect CO molecules in the  $\text{SF}_6$  matrix.

**Experimental Setup.** A schematic of the QEPAS sensor for CO detection in the  $\text{SF}_6$  matrix is depicted in Figure 5. A mid-infrared DFB QCL (AdTech Optics, model HHL-17-62) with a central wavelength of 4.61  $\mu\text{m}$  was chosen as the light excitation source (for the selection process of the CO absorption line and the selection of the light excitation source,

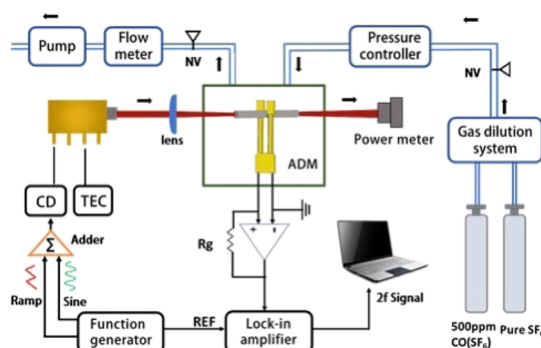
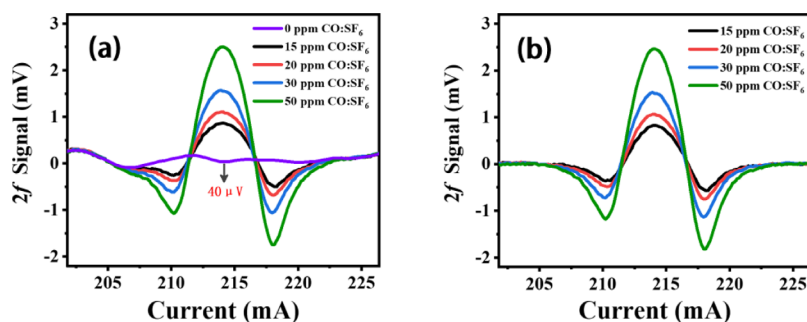


**Figure 5.** Schematic of the QEPAS sensor for CO detection in the  $\text{SF}_6$  matrix. CD, current driver; TEC, thermo-electric cooler; ADM, acoustic detection module; NV, needle valve.

see Supporting Information, Discussion S1, Figure S5). A temperature controller (Thorlabs, model TED200C) and a current driver (Wavelength Electronics, model QCL2000LAB) were used to fix the operating temperature and the injected current in the QCL, respectively. According to the HITRAN database, the R(6) CO absorption line located at 2169.2  $\text{cm}^{-1}$  with a line-strength of  $4.5 \times 10^{-19}$  cm/mol was selected in the fundamental band. To target the selected R(6) line, the temperature and the current of the DFB QCL were set to 37  $^{\circ}\text{C}$  and 214 mA, respectively: in these conditions, an optical power of 20 mW was measured. The QEPAS spectrophone composed of 8 kHz-QTF and a pair of resonator tubes ( $l = 7.5$  mm and ID = 1.0 mm) was mounted in a stainless steel gas chamber with a volume of 114  $\text{cm}^3$ , equipped with two  $\text{CaF}_2$  windows with a diameter of 25 mm, a gas inlet, and outlet connectors. The laser beam was focused into the gas cell by using a  $\text{CaF}_2$  lens in order to pass through the resonator tubes without touching them. A power meter was placed after the ADM both to align the laser beam and to monitor the optical power in real time. The QCL scanned the selected CO absorption line by applying a slow (10 mHz) ramp from 202 to 222 mA to the current driver. The QEPAS sensor operated in wavelength modulation and 2f-detection: the laser current was modulated at half of the QTF resonance frequency and the QTF signal was demodulated by using a lock-in amplifier (Stanford Research System, model SR830) at the QTF resonance frequency. The integration time of the lock-in amplifier were set to 1 s with filter slope = 12 dB/octave. The corresponding detection bandwidth was 0.25 Hz. Starting from two certified gas cylinders containing pure  $\text{SF}_6$  and a mixture of 500 ppm of CO in  $\text{SF}_6$ , different CO concentrations in  $\text{SF}_6$  were generated by using a gas dilution system. A diaphragm pump, a system of valves, a pressure controller, and a flow meter were used to fix the pressure and measure the gas flow rate within the gas line.

## RESULTS AND DISCUSSION

**Assessment of QEPAS Sensor Performance.** The performance of a QEPAS sensor depends on the amplitude of the sinusoidal modulation applied to the laser driver and on the gas pressure. The current modulation amplitude depends on the gas pressure because the fwhm of the absorption line suffers from the pressure broadening. Thus, for each gas pressure, an optimal current modulation amplitude can be expected. The QEPAS signal is proportional to the QTF quality factor, which increases as the pressure decreases (see



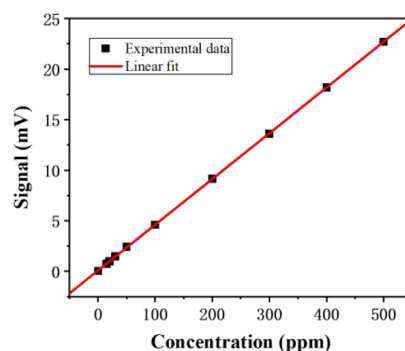
**Figure 6.** (a)  $2f$  spectra at different concentrations of CO in SF<sub>6</sub> mixture and  $2f$  signal of pure SF<sub>6</sub>, as current was swept from 202 to 226 mA. (b) Second-harmonic signal obtained by subtracting the  $2f$  signal of pure SF<sub>6</sub> from the four  $2f$ -spectra with different concentrations in (a).

Figure 4b). However, a reduction of the pressure results in a decrement of the number of molecules, negatively affecting the sound generation efficiency within the gas. These two opposite trends identify an optimal operating gas pressure.

The certified 500 ppm CO/SF<sub>6</sub> gas mixture was used to investigate the QEPAS signal as a function of the peak-to-peak modulation amplitude, for representative gas pressure values ranging from 700 to 100 Torr. For each spectral scan, the maximum value was extracted (Figure S3). The gas flow rate was fixed to 60 standard cubic centimeters per minute (sccm) for each measurement. At fixed pressure, the QEPAS signal rapidly increases as the modulation depth increases until it reaches a maximum value; then it slightly decreases. A modulation depth maximizing the QEPAS signal is well identifiable for each pressure. As the pressure decreases, the modulation depth maximizing the QEPAS signal clearly shifts toward lower values, as expected because the fwhm value of the CO absorption feature decreases as the pressure is reduced. Thus, the trend of the QEPAS signal as a function of the gas mixture pressure can be extracted. As a result of the investigation, the optimal modulation depth and gas pressure are 80 mV and 500 Torr, respectively.

Starting from the certified 500 ppm CO in the SF<sub>6</sub> mixture, different CO concentrations in SF<sub>6</sub> were generated by using a gas dilution system, down to 15 ppm of CO in SF<sub>6</sub>. High-resolution QEPAS spectral scans of CO/SF<sub>6</sub> mixtures with different concentrations are shown in Figure 6a, together with the spectral scan acquired when pure SF<sub>6</sub> flows in the QEPAS sensor.

As expected, when CO flows in the line, the acquired QEPAS scan clearly resembles the second-derivative of the Lorentzian-like R(6) CO absorption line with distortions on negative lobes caused by the residual amplitude modulation effect.<sup>40</sup> When pure SF<sub>6</sub> flows in the sensor, the spectral scan is not zero-flat, but a weak structureless absorption feature is observed, this result agrees with the observation of a flat, continuous, and weak SF<sub>6</sub> absorption background around 4.61 μm, which is discussed in the Supporting Information Discussion S1. Assuming it as a background, the pure SF<sub>6</sub> QEPAS scan was subtracted from the CO scans to filter out SF<sub>6</sub> absorption interference. In detail, at the QCL current of 214 mA, that is, where the maximum of CO absorption spectrum is located, the pure SF<sub>6</sub> signal amplitude is ~40 μV. The CO QEPAS scans after the background subtraction are shown in Figure 6b. For each spectral scan, the QEPAS peak signal was extracted and plotted as a function of the CO concentration in Figure 7.



**Figure 7.** Linear relationship of the QEPAS peak signal as a function of the CO nominal concentrations.

The sensor response curve was obtained by imposing a linear fit to the experimental data-points, characterized by an  $R^2$  value equal to 0.99995 and a slope equal to 45.1 μV/ppm. A  $1\sigma$  noise of 4.6 μV was measured at 1 s of integration time, thus a minimum detection limit of 90 ppb was estimated, corresponding to a normalized noise equivalent absorption coefficient (NNEA) of  $1.8 \times 10^{-7} \text{ W cm}^{-1} \text{ Hz}^{-1/2}$ .

The long-term stability of the CO-QEPAS sensor was investigated by performing an Allan-Werle variance analysis. Pure SF<sub>6</sub> was flushed into the gas line with the QCL wavelength locked at the CO absorption peak, while the measurement was done in ppb units by using the sensor response curve that is plotted as a function of the signal integration time, with both horizontal and vertical axes in logarithmic scale (Figure S4). For a lock-in integration time of 10 s, a minimum detection limit as low as 10 ppb was achieved. This detection sensitivity reaches the single ppb level by increasing the integration up to 100 s.

The sensor response time is the last parameter to be determined. For CO real-time monitoring in GIS, the faster the response time of the system, the earlier the failure conditions in the equipment can be known and handled. A gas cell volume as low as few cubic centimeters allows a rapid exchange of gas. In addition, a fast flow rate of SF<sub>6</sub> can positively affect the response time. However, with flow rates >60 sccm the noise level increases, and the sensor performance deteriorates. Thus, the gas flow rate was fixed to 60 sccm. The sensor response time was determined as follows. First, the QCL current was fixed to 214 mA, corresponding to the maximum of the CO absorption line. Starting from pure SF<sub>6</sub> flowing in the sensor gas line, 100 ppm CO/SF<sub>6</sub> mixture was rapidly introduced into the system. The rise time was measured as the time required for QEPAS signal to rise from the background level to 100% of



its steady value. After stabilization, the gas dilution system quickly switches again to pure SF<sub>6</sub> in order to measure the fall time, defined as the time required for the QEPAS signal to decrease from the steady-state value to the background level. Figure 8 depicts the measurement of the rise and fall response times of the CO QEPAS signal.

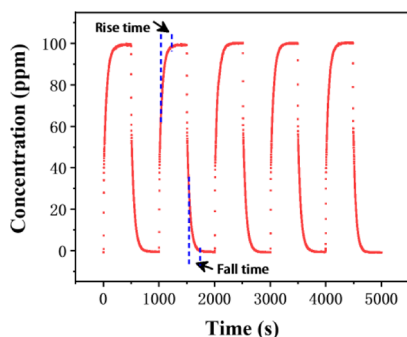


**Figure 8.** Rise time and fall time of the flow response of the CO/SF<sub>6</sub> sensor system for a CO concentration equal to 100 ppm.

An average rise and fall time of 3 min was estimated. The measurements were repeated several times and no hysteresis effects or time delays were observed.

## CONCLUSIONS

A sensitive and compact QEPAS gas sensor for the detection of CO in the SF<sub>6</sub> matrix was demonstrated, employing a spectrophone composed by custom T-shaped grooved QTF and a pair of resonator tubes. The QTF was designed to achieve a low resonance frequency of 8 kHz and a high quality factor of 6000 in the SF<sub>6</sub> matrix at atmospheric pressure. This allowed an efficient detection of the CO photoacoustic response in SF<sub>6</sub>, providing the highest QEPAS signal at an operating pressure of 500 Torr. A strong CO spectral feature located at 4.61  $\mu\text{m}$  was targeted by means of a compact DFB-QCL with an emission power of 20 mW. The SF<sub>6</sub> absorption contribution results in a weak structureless background that can be easily subtracted. The linearity of the CO sensor response was demonstrated in the range 0–500 ppm and a minimum detection limit of 90 ppb at 1 s of integration time was achieved, corresponding to a NNEA of  $1.8 \times 10^{-7} \text{ W cm}^{-1} \text{ Hz}^{-1/2}$ . A sensor response time of  $\sim 3$  min was measured when the gas flow rate is 60 sccm. The overall performances match the requirements for real-time monitoring of GIS discharge, offering a compact and reliable alternative to the bulky instruments currently employed to accomplish the task.

## ASSOCIATED CONTENT

### Supporting Information

The Supporting Information is available free of charge at <https://pubs.acs.org/doi/10.1021/acs.analchem.0c02772>.

Circuit diagram for QTF characterization; schematic diagram of the employed QEPAS spectrophone; QEPAS signal of 500 ppm of CO/SF<sub>6</sub> under different pressures and different modulation depths; Allan-Werle deviation plot for the CO-QEPAS sensor with 8 kHz-QTF in the SF<sub>6</sub> environment; and selection of CO absorption line (PDF)

## AUTHOR INFORMATION

### Corresponding Authors

**Hongpeng Wu** – State Key Laboratory of Quantum Optics and Quantum Optics Devices, Institute of Laser Spectroscopy and Collaborative Innovation Center of Extreme Optics, Shanxi University, Taiyuan 030006, China; Email: [wuhp@sxu.edu.cn](mailto:wuhp@sxu.edu.cn)

**Lei Dong** – State Key Laboratory of Quantum Optics and Quantum Optics Devices, Institute of Laser Spectroscopy and Collaborative Innovation Center of Extreme Optics, Shanxi University, Taiyuan 030006, China; [orcid.org/0000-0001-7379-3388](https://orcid.org/0000-0001-7379-3388); Email: [donglei@sxu.edu.cn](mailto:donglei@sxu.edu.cn)

**Vincenzo Spagnolo** – PolySense Laboratory, Dipartimento Interateneo di Fisica, University and Politecnico of Bari, CNR-IFN, Bari 70126, Italy; [orcid.org/0000-0002-4867-8166](https://orcid.org/0000-0002-4867-8166); Email: [vincenzoluigi.spagnolo@poliba.it](mailto:vincenzoluigi.spagnolo@poliba.it)

### Authors

**Bo Sun** – State Key Laboratory of Quantum Optics and Quantum Optics Devices, Institute of Laser Spectroscopy and Collaborative Innovation Center of Extreme Optics, Shanxi University, Taiyuan 030006, China

**Andrea Zifarelli** – State Key Laboratory of Quantum Optics and Quantum Optics Devices, Institute of Laser Spectroscopy, Shanxi University, Taiyuan 030006, China; PolySense Laboratory, Dipartimento Interateneo di Fisica, University and Politecnico of Bari, CNR-IFN, Bari 70126, Italy

**Stefano Dello Russo** – State Key Laboratory of Quantum Optics and Quantum Optics Devices, Institute of Laser Spectroscopy, Shanxi University, Taiyuan 030006, China; PolySense Laboratory, Dipartimento Interateneo di Fisica, University and Politecnico of Bari, CNR-IFN, Bari 70126, Italy

**Shangzhi Li** – State Key Laboratory of Quantum Optics and Quantum Optics Devices, Institute of Laser Spectroscopy and Collaborative Innovation Center of Extreme Optics, Shanxi University, Taiyuan 030006, China

**Pietro Patimisco** – State Key Laboratory of Quantum Optics and Quantum Optics Devices, Institute of Laser Spectroscopy, Shanxi University, Taiyuan 030006, China; PolySense Laboratory, Dipartimento Interateneo di Fisica, University and Politecnico of Bari, CNR-IFN, Bari 70126, Italy

Complete contact information is available at:

<https://pubs.acs.org/doi/10.1021/acs.analchem.0c02772>

### Author Contributions

B.S., A.Z., and H.W. contributed equally to this manuscript. B.S. performed the experiments. A.Z. and H.W. provided experiment guidance. B.S., A.Z., and H.W. wrote the manuscript. L.D. and V.S. supported the experiments and contributed to the manuscript. S.D.R., S.L., and P.P. provided technical guidance. All the authors have given approval to the final version of the manuscript.

### Notes

The authors declare no competing financial interest.

## ACKNOWLEDGMENTS

The authors from Shanxi University acknowledge the financial support by the National Natural Science Foundation of China (grant no. 61805132), program TYMIT, Shanxi “1331KSC”, 111 project (D18001), Sanjin Scholar (no. 2017QNSJXZ-04), Applied basic research program of Shanxi Province (201801D221174), and Scientific and Technological Innovation Programs of Higher Education Institutions In Shanxi

(2019L0028). The authors from Dipartimento Interateneo di Fisica di Bari acknowledge the financial support from the European Union's Horizon 2020 research and innovation programme under the Marie Skłodowska-Curie project OPTAPHI, grant no. 860808, and from THORLABS GmbH within the joint-research laboratory PolySense.

## REFERENCES

- (1) Hoshina, Y.; Hanai, M.; Shiiki, M.; Kaneko, E.; Sato, M. *IEE Proc. Sci. Meas. Technol.* **2006**, *153*, 1–6.
- (2) Ma, G.-m.; Wu, Z.; Zhou, H.; Jiang, J.; Chen, W.; Zheng, S.; Li, C.; Li, X.; Wang, Z. *IEEE Trans. Power Deliv.* **2016**, *31*, 1270–1280.
- (3) Istad, M.; Runde, M. *IEEE Trans. Power Deliv.* **2010**, *25*, 2448–2454.
- (4) Yin, X.; Dong, L.; Wu, H.; Zheng, H.; Ma, W.; Zhang, L.; Yin, W.; Xiao, L.; Jia, S.; Tittel, F. K. *Opt. Express* **2017**, *25*, 32561–32590.
- (5) Luo, J.; Fang, Y. H.; Zhao, Y. D.; Wang, A. J.; Li, D. C.; Li, Y. Y.; Liu, Y.; Cui, F. X.; Wu, J.; Liu, J. X. *Anal. Methods* **2015**, *7*, 1200–1207.
- (6) Zhang, X.; Tie, J.; Zhang, J. *Sensors* **2013**, *13*, 14764–14776.
- (7) Tang, J.; Liu, F.; Zhang, X.; Meng, Q.; Zhou, J. *IEEE Trans. Dielectr. Electr. Insul.* **2012**, *19*, 29–36.
- (8) Fan, X.; Li, L.; Zhou, Y.; Tang, N.; Zou, Z.; Li, X.; Huang, G.; Liu, M. *IET Sci. Meas. Technol.* **2018**, *12*, 707–711.
- (9) Cui, R.; Dong, L.; Wu, H.; Li, S.; Zhang, L.; Ma, W.; Yin, W.; Xiao, L.; Jia, S.; Tittel, F. K. *Opt. Express* **2018**, *26*, 24318–24328.
- (10) Yan, X. L.; Song, G.; Wang, C. Y.; Ji, Y. S.; Yang, R.; Jian, Y. F.; Liu, H. M. *Elect. Power Autom. Equip.* **2014**, *34*, 83–88.
- (11) Kórh, O.; Rikker, T.; Molnár, G.; Mahara, B. M.; Torkos, K.; Borossay, J. *Rapid Commun. Mass Spectrom.* **1997**, *11*, 1643–1648.
- (12) Casanovas, A. M.; Casanovas, J.; Lagarde, F.; Belarbi, A. *J. Appl. Phys.* **1992**, *72*, 3344.
- (13) Liu, H.; Zhou, Q.; Zhang, Q.; Hong, C.; Xu, L.; Jin, L.; Chen, W. *Sensors* **2017**, *17*, 913.
- (14) Hergli, R.; Casanovas, J.; Derdouri, A.; Grob, R.; Mathieu, J. *IEEE Trans. Electr. Insul.* **1988**, *23*, 451–465.
- (15) Yin, X.; Wu, H.; Dong, L.; Ma, W.; Zhang, L.; Yin, W.; Xiao, L.; Jia, S.; Tittel, F. K. *Sens. Actuators, B* **2019**, *282*, 567–573.
- (16) Chen, K.; Deng, H.; Guo, M.; Luo, C.; Liu, S.; Zhang, B.; Ma, F.; Zhu, F.; Gong, Z.; Peng, W.; Yu, Q. *Opt. Laser Technol.* **2020**, *123*, 105894.
- (17) Dong, L.; Kosterev, A. A.; Thomazy, D.; Tittel, F. K. *Appl. Phys. B* **2010**, *100*, 627–635.
- (18) Wu, H.; Dong, L.; Zheng, H.; Yu, Y.; Ma, W.; Zhang, L.; Yin, W.; Xiao, L.; Jia, S.; Tittel, F. K. *Nat. Commun.* **2017**, *8*, 15331.
- (19) Patimisco, P.; Sampaolo, A.; Dong, L.; Tittel, F.; Spagnolo, V. *Appl. Phys. Rev.* **2018**, *5*, 011106.
- (20) Zheng, H.; Dong, L.; Wu, H.; Yin, X.; Xiao, L.; Jia, S.; Curl, R. F.; Tittel, F. K. *Chem. Phys. Lett.* **2018**, *691*, 462–472.
- (21) Patimisco, P.; Sampaolo, A.; Zheng, H.; Dong, L.; Tittel, F. K.; Spagnolo, V. *Adv. Phys.: X* **2016**, *2*, 169–187.
- (22) Dello Russo, S.; Giglio, M.; Sampaolo, A.; Patimisco, P.; Menduni, G.; Wu, H.; Dong, L.; Passaro, V.; Spagnolo, V. *Sensors* **2019**, *19*, 4109.
- (23) Tittel, F. K.; Sampaolo, A.; Patimisco, P.; Dong, L.; Geras, A.; Starecki, T.; Spagnolo, V. *Opt. Express* **2016**, *24*, A682–A692.
- (24) Wu, H.; Dong, L.; Yin, X.; Sampaolo, A.; Patimisco, P.; Ma, W.; Zhang, L.; Yin, W.; Xiao, L.; Spagnolo, V.; Jia, S. *Sens. Actuators, B* **2019**, *297*, 126753.
- (25) Gaudiuso, C.; Volpe, A.; Ancona, A. *Micromachines* **2020**, *11*, 327.
- (26) Li, S.; Dong, L.; Wu, H.; Sampaolo, A.; Patimisco, P.; Spagnolo, V.; Tittel, F. K. *Anal. Chem.* **2019**, *91*, 5834–5840.
- (27) Patimisco, P.; Sampaolo, A.; Mackowiak, V.; Rossmadl, H.; Cable, A.; Tittel, F. K.; Spagnolo, V. *IEEE Trans. Ultrason. Ferroelectrics Freq. Contr.* **2018**, *65*, 1951–1957.
- (28) Ma, Y.; Lewicki, R.; Razeghi, M.; Tittel, F. K. *Opt. Express* **2013**, *21*, 1008–1019.
- (29) Kosterev, A. A.; Bakhirkin, Y. A.; Tittel, F. K. *Appl. Phys. B* **2005**, *80*, 133–138.
- (30) Bailey, R. T.; Cruickshank, F. R.; Guthrie, R.; Pugh, D.; Weir, I. J. M. *Chem. Phys.* **1987**, *114*, 411–416.
- (31) Richman, D. C.; Millikan, R. C. *J. Chem. Phys.* **1975**, *63*, 2242–2244.
- (32) Hanson, R. K. *AIAA J.* **1971**, *9*, 1811–1819.
- (33) Elefante, A.; Menduni, G.; Rossmadl, H.; Mackowiak, V.; Giglio, M.; Sampaolo, A.; Patimisco, P.; Passaro, V. M. N.; Spagnolo, V. *Sensors* **2020**, *20*, 2935.
- (34) Patimisco, P.; Sampaolo, A.; Giglio, M.; Dello Russo, S.; Mackowiak, V.; Rossmadl, H.; Cable, A.; Tittel, F. K.; Spagnolo, V. *Opt. Express* **2019**, *27*, 1401–1415.
- (35) Patimisco, P.; Borri, S.; Sampaolo, A.; Beere, H. E.; Ritchie, D. A.; Vitiello, M. S.; Scamarcio, G.; Spagnolo, V. *Analyst* **2014**, *139*, 2079–2087.
- (36) Blake, W. K. *J. Sound Vib.* **1974**, *33*, 427–450.
- (37) Giglio, M.; Menduni, G.; Patimisco, P.; Sampaolo, A.; Elefante, A.; Passaro, V. M. N.; Spagnolo, V. *Phys. Status Solidi A* **2019**, *216*, 1800552.
- (38) Hosaka, H.; Itao, K.; Kuroda, S. *Sens. Actuators, A* **1995**, *49*, 87–95.
- (39) Ogawa, N.; Kaneko, F. *Eur. J. Phys.* **2013**, *34*, 1159–1165.
- (40) Patimisco, P.; Sampaolo, A.; Bidaux, Y.; Bismuto, A.; Scott, M.; Jiang, J.; Muller, A.; Faist, J.; Tittel, F. K.; Spagnolo, V. *Opt. Express* **2016**, *24*, 25943–25954.